Detection of carbon dioxide leakage during injection in deep saline formations by pressure tomography

Linwei Hu[1], Peter Bayer[1], and Ralf Brauchler[2]

[1]Department of Earth Sciences, ETH Zurich, Zurich, Switzerland, [2]AF-Consult Switzerland Ltd., Baden, Switzerland
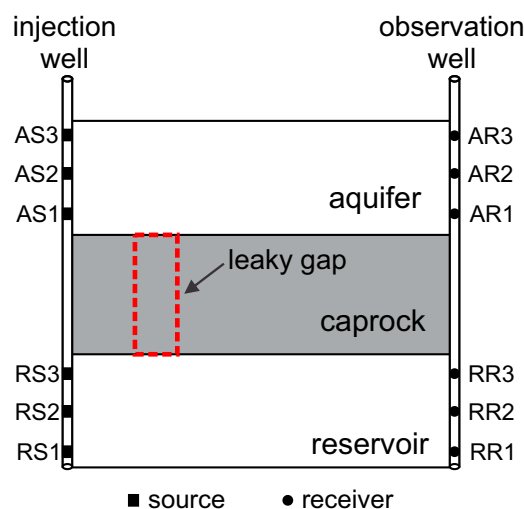
Abstract CO_2 injected into storage formations may escape to the overlying permeable layers. Mixed-phase diffusivity, namely the ratio of hydraulic conductivity and specific storage of the phase mixture, declines with increasing CO_2 saturation. Thus, it can be an indicator of CO_2 leakage. In this study, we perform interference brine or CO_2 injection tests in a synthetic model, including a storage reservoir, an above aquifer, and a caprock. Pressure transients derived from an observation well are utilized for a travel-time based inversion technique. Variations of diffusivity are resolved by inverting early travel time diagnostics, providing an insight of plume development. Results demonstrate that the evolution of CO_2 leakage in the above aquifer can be inferred by interpreting and comparing the pressure observations, travel times, and diffusivity tomograms from different times. The extent of the plume in reservoir and upper aquifer are reconstructed by clustering the time-lapse data sets of the mixed-phase diffusivity, as the diffusivity cannot be exactly reproduced by the inversion. Furthermore, this approach can be used to address different leaky cases, especially for leakage occurring during the injection.

1. Introduction

Deep saline aquifers are deemed most suitable for geological CO_2 storage [*Bachu and Adams*, 2003]. However, injection of CO_2 in deep reservoirs is not free of risks. An evolving plume might migrate to overlying strata along unknown seal imperfections, faults or fractures in caprocks, or preexisting abandoned wells [*Lemieux*, 2011]. Also, the high pressures during injection can create new pathways for escape. When CO_2 emanating from storage formations reaches shallow aquifers, it contaminates the groundwater environment [*Apps et al.*, 2010]. Therefore, identification of possible CO_2 leakage is a crucial task during sequestration. Monitoring needs to localize weak zones in a caprock and migration pathways to be able to plan countermeasures.

Pressure-based techniques are appealing for early stage leakage detection, since pressure perturbations propagate much faster than a CO_2 plume itself. In previous work, mainly synthetic models are utilized to assess the impact on pressure buildup due to brine/CO_2 leakage [e.g., *Birkholzer et al.*, 2009] and detectability of brine/CO_2 leakage through leaky wells or permeable caprock based on pressure transients in the storage reservoir and its overlying aquifer [e.g., *Chabora and Benson*, 2009; *Nogues et al.*, 2011; *Azzolina et al.*, 2013; *Wang and Small*, 2014]. Forward modeling can be done by fully coupled numerical simulators, or by simplified analytical or semianalytical solutions [e.g., *Nordbotten et al.*, 2004, 2008; *Celia and Nordbotten*, 2009; *Zhou et al.*, 2009; *Cihan et al.*, 2011]. By comparison to simulation results, pressure observations at a field site can be interpreted [e.g., *Park et al.*, 2012].

Alternatively, leakage locations, rates, and permeability of leaky wells are inferred by inverting pressures and calibrating forward models. Most studies in this field utilize the pressure anomalies in the storage formation or the above aquifer for the inversion, which requires knowledge of pressure responses in a no-leakage case [e.g., *Sun and Nicot*, 2012; *Jung et al.*, 2013; *Lee et al.*, 2015]. The leakage amount can be estimated by historical matching of pressure data to analytical solutions [e.g., *Meckel et al.*, 2013; *Hosseini*, 2014]. However, such simplified approaches may not be satisfactory for complex geometries. Also, none of the available pressure-based inversion techniques can provide spatial information of an evolved secondary CO_2 plume in the above-zone, which is fundamental for the planning of remediation strategies. To date, only seismic reflection tomography is utilized for mapping a leaky plume [e.g., *Arts et al.*, 2005; *Chadwick et al.*, 2014]. However, its spatial resolution and coverage is limited.

injection well   observation well

AS3 · AR3

AS2 · AR2   aquifer

AS1 · AR1

leaky gap

caprock

RS3 · RR3

RS2 · RR2   reservoir

RS1 · RR1

■ source   ● receiver

Figure 1. Schematic sketch of the conceptual model. Distance between two wells is 50 m, and the thickness of each layer is 15 m. AS1–AS3 and RS1–RS3 imply the installed sources in the aquifer and reservoir, respectively, while AR1–AR3 and RR1–RR3 indicate the corresponding receivers in the monitoring well. Red dashed line sketches the area of fracture leakage (case F).

Hydraulic, or more generally, pressure tomography has been developed during the last decades as an approach to reconstruct the subsurface heterogeneity. Its applicability in single-phase flow field has been demonstrated successfully by numerical models [e.g., *Yeh and Liu*, 2000], laboratory experiments [e.g., *Illman et al.*, 2010], and field-scale tests [e.g., *Brauchler et al.*, 2013]. *Hu et al.* [2015] proposed a pressure-based tomographical approach to track the evolution of a CO_2 plume in a homogeneous storage reservoir. They characterized the CO_2-induced heterogeneity of hydraulic properties and delineated the plume shape by the comparison of diffusivity tomograms in a time-lapse strategy. The objective of this paper is to introduce this pressure-based tomographical approach to characterize potential CO_2 leakages in a multilayer system with a storage formation, an above aquifer, and an intervening caprock. Repetition of pressure tomography prior to, and after CO_2 injection, enables continuous monitoring of the CO_2 plume and potential leakage between the well pair. Contrary to other pressure-based inversion methods, this approach requires merely short-duration pressure transients and it can be applied for multiple leakage cases occurred after CO_2 injection. The multilayer system is initially saturated with brine, and brine displacement is not considered in this work. In the following sections, a novel design of interference fluid tests applied to the storage formation and the above aquifer is proposed. The observed pressure data at the monitoring well is utilized for inverting the spatial distribution of diffusivity in tomograms and evolving plumes in the two permeable layers are determined by clustering the tomograms.

2. Methodology

2.1. Problem Set-up

A synthetic case is set up in a numerical model. We utilize an open source code, PFLOTRAN [e.g., *Hammond et al.*, 2014], for the forward simulation of the two-phase, two-component, and nonisothermal transport processes. For the forward model, the CO_2 storage formation, the overlying monitoring zone, and the caprock are considered as an entirely confined system (Figure 1). Following the suggestions by *Sun et al.* [2015], the storage formation is named the "reservoir" and the monitoring zone above the caprock is the "aquifer." The bottom of the simulated example is 1600 m below the ground surface. Reservoir and aquifer are composed of sandstone, whereas the material of the caprock is shale or siltstone. Each layer is assumed homogeneous and isotropic, with an equivalent thickness of 15 m. Pressure at the bottom is assigned a value of 14.7 MPa, with a constant vertical pressure gradient of 0.01 MPa/m. No-flow conditions are assigned to the top and bottom of the system, while the grids at the distant boundaries are set to a constant hydrostatic pressure. The initial system is stagnant and fully saturated with brine, with a constant temperature of 65°C. Under these conditions, CO_2 is in supercritical state.

The entire system is simulated in a simplified two-dimensional cross-sectional model with nonuniform rectangular grids. A three-dimensional and nonuniform plume could be identified by increasing the number of the wellbores and performing the injection tests in different wellbores. The lateral extent (*x*-direction) of the model is 560 m. An injection well with a radius of 0.09 m is placed at the center of the model domain, completely penetrating the three formations. Two observation wells are located 50 and 100 m away from the injection well to monitor the pressure responses, which are comparable to the distance of well pairs in several pilot sites [e.g., *Wiese et al.*, 2010; *Niemi et al.*, 2012]. The model comprises 45 layers, each with a constant thickness of 1 m. The lateral discretization is set to 1 m between the wells, with a progressive refinement to 0.09 m toward the injection well. Outside of the area constrained by the well pair, the

Table 1. Summary of Model Parameter Values for Three Cases

Parameter	Case	Unit	Reservoir	Aquifer	Seal Unit	Leaky Gap (in Case F)
Intrinsic permeability	N	m^2	1×10^{-13}	1×10^{-13}	1×10^{-19}	n.a.
	F				1×10^{-19}	1×10^{-11}
	D				1×10^{-14}	n.a.
Entry pressure	N	Pa	8×10^3	8×10^3	3.9×10^6	n.a.
	F				3.9×10^6	1×10^3
	D				1.2×10^4	n.a.
Effective porosity	All		0.25	0.25	0.05	0.25
Pore size distribution	All		1.5	1.5	0.5	1.5
Specific heat capacity	All	J/kg K	860	860	830	860
Dry thermal conductivity	All	W/m K	2.6	2.6	1	2.6
Wet thermal conductivity	All	W/m K	4.6	4.6	1.8	4.6
Rock density	All	kg/m^3	2600	2600	2700	2600
Initial temperature	All	°C			65	
Salinity	All	g/l			67	
Gravitational acceleration	All	m^2/s			9.81	
Residual saturation of wetting phase	All				0	
Residual saturation of nonwetting phase	All				0	
Initial datum pressure	All	MPa			14.7	
Diffusion coefficient of dissolved CO_2 in brine	All	m^2/s			3×10^{-9}	

horizontal grid resolution is increased exponentially. The largest grid size is at the distant boundaries with a value of 30 m. Ultimately, a discretization of $322 \times 45 = 14,490$ grid cells in total is created.

2.2. Leaky Cases and Model Parameters

On the premise that the structure of the three-layer system is characterized by previous site investigation before the CO_2 injection campaign starts, we distinguish three different cases: "case N", "case F", and "case D". The presumptive model parameters of these three cases are summarized in Table 1. Case N refers to a no-leakage case with a caprock of permeability $k = 1 \times 10^{-19}$ m^2. Simulation results of this case serve as a reference for comparison with the two other leaky cases. Case F implies a case of unanticipated fracture leakage in the caprock, which is caused by any potential excitation, such as overpressure by CO_2 injection, or a seismic event. We suppose the creation of a leaky pathway occurred at 350 h after the depth-integrated CO_2 injection. New pathways evolve, reflected in a discontinuity in the caprock. For convenience, a rectangle gap is assigned as a leaky path (Figure 1) with a moderate permeability value of 1×10^{-11} m^2. Case D simulates diffusive leakage. In this case, CO_2 may migrate through the seal unit, of which the sealing capacity prior to CO_2 injection is assumed to be overestimated. Effective permeability of the seal unit is set at a relatively high value of 1×10^{-14} m^2. This case can be used for CO_2 leakage through small intraformation shale layers as a more realistic condition.

For all cases, the intrinsic permeability of the reservoir and aquifer equals 1×10^{-13} m^2. Rock density and effective porosity of the two permeable layers and the leaky gap are 2600 kg/m^3 and 0.25, respectively, and they are set to 2700 kg/m^3 and 0.05 for the caprock. The heat capacity and the dry and wet rock thermal conductivity of the permeable units (reservoir, aquifer, and leaky gap) are 860 J/kg, 2.6 W/mK, 4.6 W/mK, and 830 J/kg, 1 W/mK, 1.8 W/mK for the caprock. A value of 67 g/l specifies the initial salinity of the reservoir. The Brooks-Corey-Burdine model [*Brooks and Corey*, 1964; *Burdine*, 1953] is employed for calculating the relative permeability and capillary pressure according to the CO_2 saturation. For the scope of this study, residual saturation of the two phases is neglected to minimize model complexity. The pore size distribution is assigned values of 1.5 for the permeable units and 0.5 for the caprock, respectively. The entry pressure of the low-permeability caprock is at a high value of 3.9×10^6 Pa, and equals 1.2×10^4 Pa for the high-permeability caprock. The entry pressure of the two permeable formations and the leaky gap is 8×10^3 Pa and 1×10^3 Pa, respectively.

2.3. Fluid Interference Tests

Cross-well fluid injection tests are conducted in a tomographic configuration. In the reservoir and aquifer, three intervals (sources) with a screen of 1 m are set up for multilevel brine/CO_2 injection tests (Figure 1). The observation points (receivers) are placed at the same depths and record the transient pressure signals continuously. The distance between two sources or receivers is 5 m. For better distinction, the sources are

named as RS1–RS3 in the reservoir and AS1–AS3 in the aquifer. Correspondingly, the receivers are named as RR1–RR3 and AR1–AR3. In analogy to the work of *Hu et al.* [2015], the fluid injection tests are designed in four stages as following:

Stage 1: Cross-well multilevel brine injection tests. At this stage, we conduct six brine injection tests in the initially CO_2-free formations. First, brine is injected from AS1 to AS3 sequentially, and then from RS1 to RS3 with a constant injection rate of 0.01 kg/s. The injection sequence is not influential to the inversion. Duration of each injection test is 0.2 h, following a recovery period of 10 h between two subsequent injections. Pressure returns to the initial conditions after each recovery test. Note that we do not consider different salinities in the reservoir and aquifer. This could be simulated but is not crucial for the presented inversion procedure.

Stage 2: CO_2 injection. After stage 1, the CO_2 sequestration phase is simulated. Here we assume the injected CO_2 is in supercritical state, and it is injected at a constant rate of 0.012 kg/s over the entire thickness of the reservoir to create a two-phase system. We distinguish two different injection durations referred to as "short injection" and "long injection", lasting 250 h and 500 h, respectively.

Stage 3: Shut-in period. At this stage, the injection is suspended and pressure falls off to its original status. The shut-in duration for short and long injection is 120 h and 250 h, respectively. It is possible to calibrate saturations by adding this stage, and in reality, it can be considered as a period for preparing the following hydraulic or other geophysical tests.

Stage 4: Cross-well multilevel brine/CO_2 injection tests. Brine is injected first in the aquifer from AS1 to AS3. Subsequently, CO_2 is injected in the reservoir from RS1 to RS3. Pressures derived at this stage are used for inverting the plumes in both reservoir and aquifer. All brine or CO_2 injection tests are executed at a constant rate of 0.01 kg/s. The duration of each injection and recovery test is defined based on two principles:

a. The injection rate has to be sufficiently large and the injection period has to be long enough to generate a pressure response, with a sufficient signal-to-noise ratio. However, a premise of this is that the injection should not induce large disturbance in the reservoir or aquifer.
b. Travel times can be delayed by nonuniform pressure buildup or heterogeneity of the formation. In the reservoir, travel times are mainly determined by the CO_2-induced heterogeneities. On the contrary, the travel times in the aquifer are influenced by both nonuniform pressures and potential leaks. For resolving small leaks with lower CO_2 saturations, the recovery period in the aquifer should be longer than in the reservoir. However, complete recovery of the pressure is almost impossible since full recovery needs much more time. Hence, here the recovery in the aquifer is terminated as the pressure reaches a quasi-steady state.

Hence, different injection and recovery durations are assigned at this stage, and the injection is halted as soon as the travel times (i.e., the time relates to the maximum pressure changes) can be noticeably identified. The duration of the injections depends also on the changes of the initial system, i.e., CO_2 enters and expands in the reservoir and aquifer. During short injection, for the three cases, durations of injection tests in the aquifer and reservoir are set to 0.2 and 3.5 h, and recovery tests last 8 and 3.5 h. During long injection, injection tests of brine sustain 0.2, 1, and 1 h for each of the cases N, D, and F, respectively. Injection and recovery tests of CO_2 in the reservoir are assigned equivalent durations, such as 5, 4, and 4.5 h for cases N, D, and F.

2.4. Inversion in Two-Phase System

Pressure responses derived from stages 1 and 4 are used for the inversion. We utilize a single-phase proxy to apply a travel time based inversion method [*Vasco et al.*, 2000; *Brauchler et al.*, 2003]. In a CO_2-brine system, considering CO_2 and brine as a phase mixture, the mixed-phase diffusivity, D, is defined as [*Hu et al.*, 2015]:

$$D = \frac{K}{S_s} = \left(\frac{k}{\phi}\right)\left[\frac{\frac{k_{rw}}{\mu_w}\rho_w + \frac{k_{rn}}{\mu_n}\rho_n}{(S_w c_w + S_n c_n)(S_w \rho_w + S_n \rho_n)}\right] \tag{1}$$

where K and S_s are the mixed-phase conductivity and specific storage. k is the intrinsic permeability, ϕ is the effective porosity. k_r, ρ, μ, S, c represent the relative permeability, density, viscosity, saturation, and

compressibility. The subscripts w and n indicate wetting phase (brine) and nonwetting phase (CO_2) respectively. S_s can rise by two orders of magnitude as S_n increases, whereas K varies nonmonotonically with S_n, and its variance is within one magnitude [*Hu et al.*, 2015]. Hence, D rapidly decreases according to the augmented S_n at the beginning, and then increases slowly as S_n reaches a certain value (see supporting information Text S1). Overall, D during the postinjection phase is smaller than its initial value, and it can be inverted by travel time diagnostics. The travel times relate to the diffusivity by a line integral:

$$\sqrt{t_{\alpha,d}} = \frac{1}{\sqrt{6f_{\alpha,d}}} \int_{x_1}^{x_2} \frac{ds}{D(s)} \tag{2}$$

where s is the propagation path, x_1 and x_2 are the injection and observation point, respectively. $f_{\alpha,d}$ is a conversion factor defined as $-W\left(\frac{\alpha_d^{2/3}}{e}\right)$. W is Lambert's W function, and α_d relates to the ratio of the first time-derivative of the space-time pressure data to the first time-derivative of the maximum value. If $f_{\alpha,d}$ equals 1, then the travel time is the peak time corresponding to the maximum time-derivative value. In analogy to seismic travel time inversion, spatial diffusivity can be resolved by an eikonal solver in a computationally efficient way. Considering that the early time diagnostics resolve the preferential flow better, the 20% travel time diagnostics (t-20%) are used in this study for the inversion following *Hu et al.* [2015]. Derived travel time diagnostics are perturbed with 1%-Gaussian noise for assessing the impact of noise associated with field data. The noise level is assumed the same as that of the seismic travel times, which are derived from a comparable setup [*Ajo-Franklin et al.*, 2013]. Potential noise can be caused, for example, by measurement errors due to different pressure devices and techniques.

2.5. Clustering

The limits of the inversion approach discussed in *Hu et al.* [2015] show that derived absolute values of diffusivity are often not comparable among different tomograms. This applies also to tomograms taken at the same time but separately for reservoir and aquifer. Therefore, following the travel time inversion, we partition the diffusivity tomograms of the reservoir and aquifer separately into two clusters by k-means clustering. Ideally, one cluster represents the plume and the other, the ambient formation. In contrast to the traditional k-means approach, the centroid of each cluster is determined by fitting the inverted logarithm diffusivities with a mixture of two Gaussian functions. Clustering will define the plume shape in the reservoir, as well as the extent of the secondary plume in the aquifer. Furthermore, the clustered structure can be utilized for acquiring saturations by a sequential and zonal calibration procedure, with the knowledge of initial flow properties. Further details can be found in *Hu et al.* [2015].

3. Result and Discussions

In this section, we only show and discuss the results of the 50 m well pair. Results and discussion of a 100 m doublet can be found in the supporting information (Text S3).
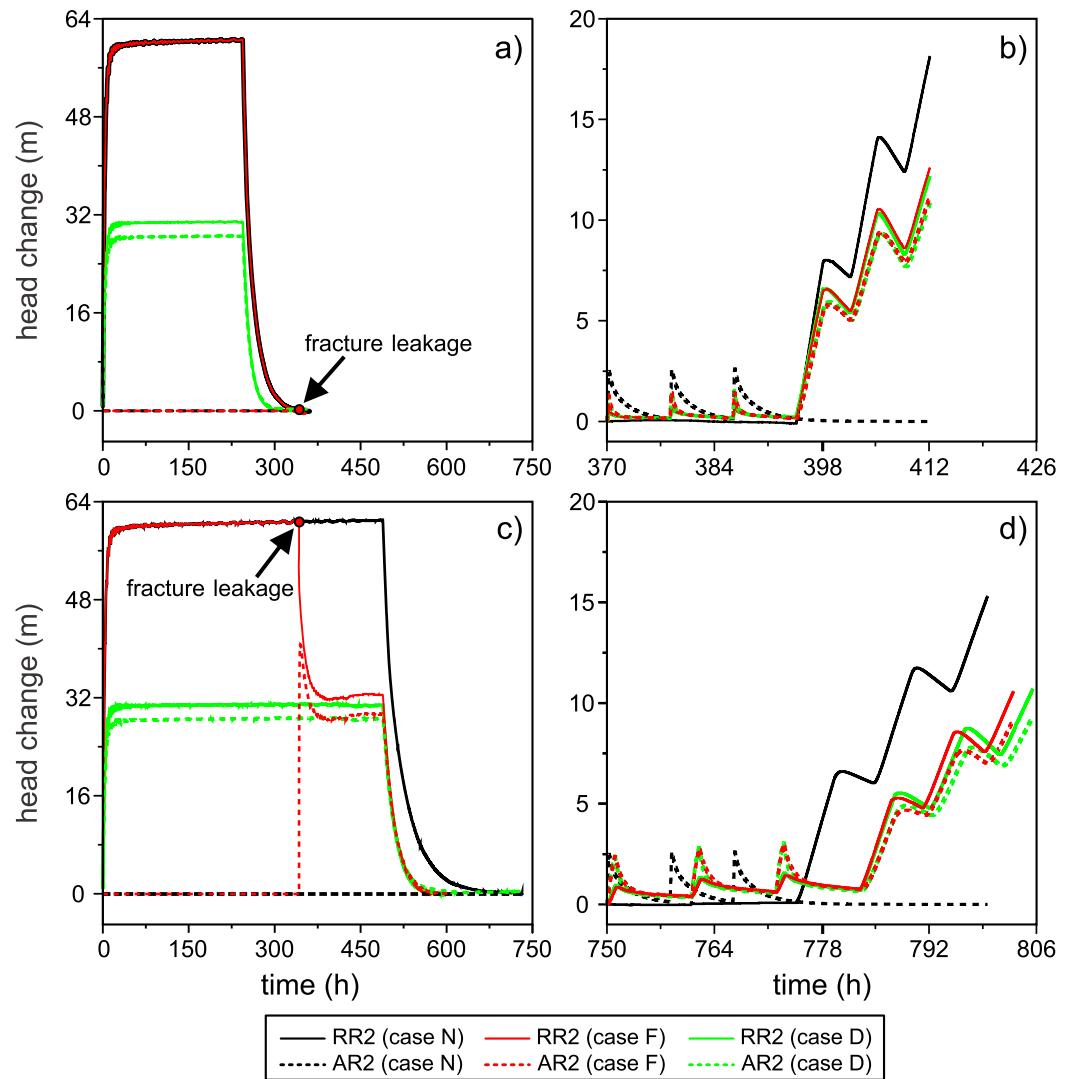
3.1. Head Changes

Here we examine direct observations and insight from forward modeling by comparing the different responses during stages 2–4, given one intact and two leaky caprocks. Pressure data in stage 1 are merely available in case N for deriving the reference travel times and inverting the CO_2-free formations, thus it is not presented. For inspection of results, we transfer the pressure data to head change (Δh) by:

$$\Delta h = \frac{\Delta P_w}{\rho_w g} \tag{3}$$

where ΔP_w is the difference between the transient pressure data and the initial hydrostatic pressure, ρ_w is the density of brine, and g denotes gravitational acceleration.

The simulated head changes are almost equivalent at RR1–RR3, as well as those among AR1–AR3. Therefore, only the observations in RR2 and AR2 are displayed. As shown in Figures 2a and 2c, at the onset of depth-integrated CO_2 injection in the reservoir, the head change Δh in the reservoir rises sharply and then reaches a quasi-steady state. In case N, as expected, pressure does not propagate through the very low-permeability caprock, and there are no responses observed in the aquifer. In case F, Δh presents similar changes as in

Figure 2. Head changes in the reservoir and aquifer at: (a) stages 2–3 during short injection; (b) stage 4 during short injection; (c) stages 2–3 during long injection; (d) stage 4 during long injection. The red dot indicates the time when an acute fracture leakage event occurred.

case N during short injection (Figure 2a). However, the fracture leakage cannot be recognized yet since it occurs almost at the end of stage 3 when pressure falls to a low level. In reality, this acute leakage may be due to a seismic event happening at the recovery period or when CO_2 injection is suspended. During long injection, Δh shows a sudden dropoff in the reservoir when the leaky gap is created due to the high pressure. Simultaneously, Δh increases rapidly in the aquifer. After the acute event, Δh arrives at a new steady state again. In case D, due to the pressure released permanently across the permeable seal, head changes are observed in both the reservoir and aquifer. Thus, comparison of results for the different cases could indicate the type of leakage.

Figures 2b and 2d show the head changes at stage 4. Δh rises first in the aquifer as brine is injected. In case N, injections in the aquifer or reservoir do not cause fluctuations in the reservoir for two injection periods. In contrast, in the two leakage cases, the leakage can be recognized by the responses in the aquifer. Δh then falls back to quasi-steady state for all cases, without a full recovery. After a certain period, CO_2 is injected into the reservoir, and Δh increases rapidly. Similarly, there are no perturbations in the aquifer in case N, whereas responses are observed in the aquifer in cases F and D. However, in the reservoir, the given time is not sufficient for recovering to steady state.

Table 2. Computed Values of t-20% of Different Source-Receiver Configurations in Aquifer and Reservoir

|	Source	Receiver	Preinjection	Case N		Case F		Case D	
				Short Injection	Long Injection	Short Injection	Long Injection	Short Injection	Long Injection
Aquifer	AS1	AR1	39.01	38.81	38.84	36.67	43.19	37.22	45.50
		AR2	39.01	38.96	38.86	36.64	43.05	37.06	45.31
		AR3	39.01	38.96	38.86	36.61	42.94	36.98	45.22
	AS2	AR1	39.01	38.99	38.94	36.59	41.77	37.33	36.02
		AR2	39.01	38.96	38.94	36.56	41.63	37.14	35.80
		AR3	39.01	38.99	38.94	36.53	41.48	37.06	35.70
	AS3	AR1	39.01	38.96	38.91	36.45	40.65	37.33	34.70
		AR2	39.01	38.96	38.91	36.40	40.53	37.14	34.50
		AR3	39.01	38.96	38.91	36.37	40.39	37.04	34.39
Reservoir	RS1	RR1	39.01	58.13	63.75	57.61	60.10	53.21	53.90
		RR2	39.01	58.17	63.94	57.66	60.18	53.41	54.19
		RR3	39.01	58.20	64.12	57.71	60.26	53.76	54.66
	RS2	RR1	39.01	96.53	132.23	103.36	113.47	95.81	116.57
		RR2	39.01	96.55	132.33	103.38	113.55	96.19	117.16
		RR3	39.01	96.56	132.46	103.41	113.60	96.93	118.24
	RS3	RR1	39.01	121.86	155.04	131.92	139.27	125.38	145.72
		RR2	39.01	121.87	155.11	131.93	139.29	125.82	146.22
		RR3	39.01	121.87	155.18	131.94	139.34	126.68	147.19

3.2. Early Time Diagnostics

We computed the early travel time diagnostics (t-20%) by differentiating pressures in stages 1 and 4 of three cases, and compare them, respectively (Table 2). Note, the diagnostics we present here have been multiplied by the conversion factor $f_{\alpha,d}$ and then squared. At stage 1, t-20% are equivalent for all the source-receiver configurations with a value of 39.01 $s^{0.5}$, which indicates the initial homogeneity of reservoir and aquifer. At stage 4, diagnostics in the reservoir show a similar trend for the three cases. Values of t-20% are small when CO_2 is injected at RS1, and they are largest at RS3. Further comparison among travel time diagnostics during short and long injections in each case indicates that the CO_2 saturation in the reservoir increased the fastest in case N and the slowest in case F. During the short injection, t-20% are smaller in the leakage cases when compared to case N. This is because the entire system is different for the three cases. In case N, the seal unit has a very low-permeability and in case D, its permeability is even higher. In case F, at the beginning of multilevel brine injection tests, the leaky gap appears in the caprock, changing its effective permeability. Diagnostics in the aquifer also provide a first insight about leakage. In case N, observed minor changes in t-20% implies that the aquifer can be considered as homogeneous. On the contrary, once CO_2 enters the aquifer in cases F and D, values of t-20% show significant variations during long injection. Since the travel time diagnostics show a relatively large variance when compared to the noise, the diagnostics derived from the reservoir when CO_2 is injected are comparable to noise-free data. In contrast, in the aquifer where no CO_2 exists, the noise level is more relevant (see the supporting information Table S1).

3.3. Inversion and Clustering

The inversion is merely based on the travel times rather than on the simulated pressures. Consequently, there is no additional flow simulation required during the inversion. Diffusivity was derived by solving equation (2) utilizing a stagger grid technique [*Böhm and Vesnaver*, 1996]. This technique can improve the resolution of the final inversion tomogram and alleviate the inversion anomalies caused by grid positions. A model with three rows and three columns was initially set up for the inversion according to the available source-receiver configurations. Sequentially, 23 inversion models were created by shifting the initial model in the horizontal and vertical directions by 7 and 2 times, respectively. The final tomogram was determined by averaging the values of each inversion result with a better resolution of 24 rows and 12 columns. Details on the inversion procedure are shown in the supporting information (Text S2).

From forward simulations, the derived saturation distributions are considered as the "truth" (Figure 3a). The maximum saturation of CO_2 in case N is 0.61 during short injection and 0.67 during long injection. The CO_2 plume does not breach the caprock in this case. During the long injection in case F, the leaky path is created. The tip of the plume migrates toward the highly permeable path, and CO_2 assembles at the boundary between the leaky gap and the aquifer. The maximum saturation at the top of the leaky gap reaches 0.86,
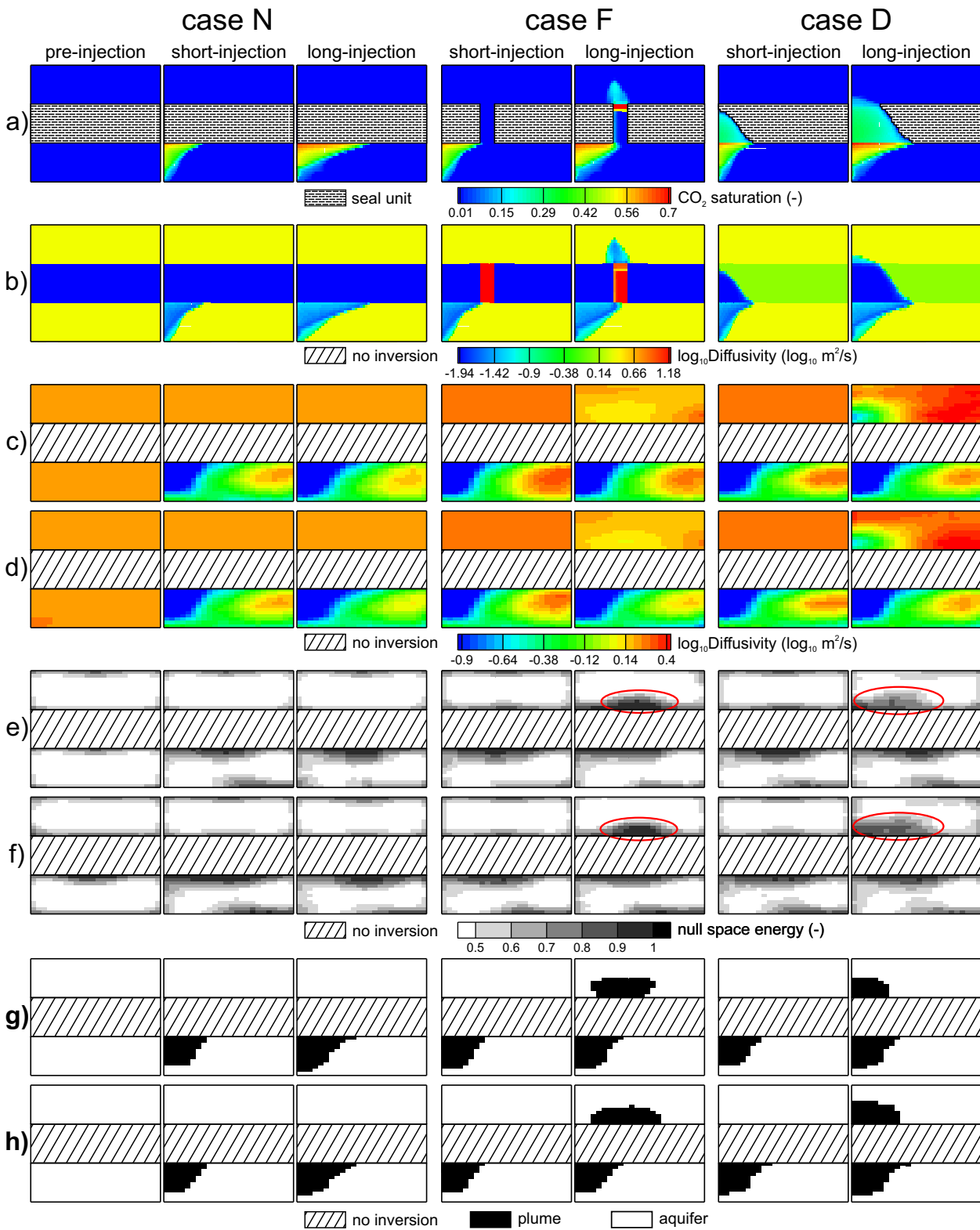
Figure 3. (a) "true" CO_2 saturation; (b) "true" diffusivity transferred from "true" CO_2 saturation; (c) inverted diffusivity (noise-free); (d) inverted diffusivity (1% noise); (e) reliability map (noise-free); (f) reliability map (1% noise); (g) clustered structure of preinjection, short injection, and long injection periods of three cases (noise-free); (h) clustered structure of the preinjection, short injection, and long injection periods of three cases (1% noise).

and CO_2 is released to the aquifer, driven by buoyancy effects. Simultaneously, the plume in the reservoir extends slower than in case N. In case D, CO_2 migrates upward through the permeable seal, with a maximum saturation value of 0.62 for short and 0.68 for long injection. The plume size in the reservoir is smaller than that in cases N and F during the short injection, and it is between the size observed in cases N and F during the long injection (because of abrupt leakage in case F). During the long injection in case D, the plume reaches the upper aquifer, inducing a secondary plume.

Figure 3b presents the mixed-phase diffusivity transferred by equation (1). Original diffusivity of the reservoir and aquifer is 2.46 m²/s, and the low-permeability seal is reflected by 1.2×10^{-5} m²/s. Diffusivity value of the leaky gap is 246 m²/s, and it is 1.22 m²/s for the relatively high-permeability seal unit in case F. Injected and leaky CO_2 alters the diffusivity by two orders of magnitude. The minimum diffusivity values are not at the front of the plume, since diffusivity does not change monotonically with CO_2 saturation [*Hu et al.*, 2015]. In cases N and F, the minimum diffusivity is around 0.02 m²/s, corresponding to a saturation of 0.31. In case D, the minimum diffusivity is around 0.01 m²/s, appearing in the caprock where the saturation is 0.25. CO_2 entered into the seal unit in this case due to its unexpectedly high permeability thus reducing the diffusivity of the seal by a factor of around 2.

Based on the travel times derived from stages 1 and 4, the inverted diffusivity tomograms are shown in Figure 3c. Diffusivity of the caprock is not determined as there is no pressure information from the caprock. The blue areas in the tomograms (Figure 3c) indicate a decrease of diffusivity caused by higher CO_2 saturations. Overall, inverted diffusivity varies from 0.01 to 2.9 m²/s, and these values are not within the range of the "true" values. This discrepancy is expected to be mainly caused by inaccuracies of the single-phase proxy and by the nonuniform trajectory distribution. Locally, small trajectory density masks small information content, and thus results in a poorly posed inversion problem. However, the small diffusivity values in the tomograms still provide structural information and thus insight into plume evolution. In the three cases, the inverted diffusivity values in the reservoir are much larger than those in the aquifer due to the larger variance of travel times derived in the reservoir. The inverted diffusivity values of the aquifer show minor changes during the short injection, which indicates a homogeneous distribution and no disturbance. During the long injection, the diffusivity in the aquifer shows a decrease when the leakage occurs in cases F and D. Figures 3e and 3f show the reliability maps, which are discussed in the supporting information (Text S4). In this study, only three sources and receivers are applied, leading to a relatively high null space energy distribution. Therefore, these reliability maps are utilized mainly as a reference for the inverted flow field, but not for the following clustering procedure.

For obtaining the plume shape, a k-means clustering method was applied (Figure 3d). The plumes identified in cases N and D grow with time, while in case F, plume shapes are similar for different injection periods. This is consistent with the conditions simulated for the "truth." As the most striking feature, the secondary plumes in the aquifer are also characterized by the clustering. Although the results imply that the plume extents are slightly overestimated, they still could provide information on the leakage type, potential position, and migration paths. The inversion results and reliability maps of 1%-noise data are similar to the noise-free data for delineating the plume shape. Slight differences due to this noise level can thus be neglected. However, in case F, increase of the distance between the two wells reduces the trajectory density of the travel time data set, weakening the detectability of the leaky plume in the upper aquifer by adding noise (supporting information Figure S4, lines d and h). This can be overcome by increasing the number of measurements. In addition, the secondary CO_2 plume in the aquifer above can be diluted by the ambient groundwater flux or hydraulic activities in the aquifer, which may hamper detecting especially small leaks.

4. Conclusions

A rapid pressure-based inversion approach is proposed for detecting CO_2 leakage through the innovative tomographical setup of fluid injection tests. It can be adapted to various cases of CO_2 leakage without previous determination of possible leaky locations. CO_2 leaking into the caprock and upper aquifer retards the plume development in the storage formation, which can be reflected through the comparison of inverted diffusivity tomograms. In comparison to previous pressure-based approaches, which mainly focus on the preexisting leaky paths, it is now also possible to find the leaky location and approximately

delineate the spreading area of leakage in different times by the inverted plumes in the above aquifer. Results indicate that pressure tomography is more suitable for identifying small-scale leaks, which might occur near the CO_2 injection well. Still, the influence of formation heterogeneity will be explored in future work.

References

Ajo-Franklin, J. B., J. Peterson, J. Doetsch, and T. M. Daley (2013), High-resolution characterization of a CO_2 plume using crosswell seismic tomography: Cranfield, MS, USA, *Int. J. Greenhouse Gas Control*, *18*, 497–509, doi:10.1016/j.ijggc.2012.12.018.

Apps, J. A., L. Zheng, Y. Zhang, T. Xu, and J. T. Birkholzer (2010), Evaluation of potential changes in groundwater quality in response to CO_2 leakage from deep geologic storage, *Transp. Porous Media*, *82*(1), 215–246, doi:10.1007/s11242-009-9509-8.

Arts, R., A. Chadwick, and O. Eiken (2005), Recent time-lapse seismic data show no indication of leakage at the sleipner CO_2-injection site, *Greenh. Gas Control Technol.*, *1*, 653–660, doi:10.1016/B978-008044704-9/50066-5.

Azzolina, N. A., M. J. Small, D. V. Nakles, and G. S. Bromhal (2013), Effectiveness of subsurface pressure monitoring for brine leakage detection in an uncertain CO_2 sequestration system, *Stochastic Environ. Res. Risk Assess.*, *28*(4), 895–909, doi:10.1007/s00477-013-0788-9.

Bachu, S., and J. J. Adams (2003), Sequestration of CO_2 in geological media in response to climate change: Capacity of deep saline aquifers to sequester CO_2 in solution, *Energy Convers. Manage.*, *44*(20), 3151–3175, doi:10.1016/S0196-8904(03)00101-8.

Birkholzer, J., Q. Zhou, and C. Tsang (2009), Large-scale impact of CO_2 storage in deep saline aquifers: A sensitivity study on pressure response in stratified systems, *Int. J. Greenhouse Gas Control*, *3*(2), 181–194, doi:10.1016/j.ijggc.2008.08.002.

Böhm, G., and A. Vesnaver (1996), Relying on a grid, *J. Seism. Explor.*, *5*(2), 169–184.

Brauchler, R., R. Liedl, and P. Dietrich (2003), A travel time based hydraulic tomographic approach, *Water Resour. Res.*, *39*(12), 1370, doi:10.1029/2003WR002262.

Brauchler, R., R. Hu, L. Hu, S. Jiménez, P. Bayer, P. Dietrich, and T. Ptak (2013), Rapid field application of hydraulic tomography for resolving aquifer heterogeneity in unconsolidated sediments, *Water Resour. Res.*, *49*, 2013–2024, doi:10.1002/wrcr.20181.

Brooks, R. H., and A. T. Corey (1964), Hydraulic properties of porous media, in *Hydrology Papers*, Colo. State Univ., Fort Collins, Colo.

Burdine, N. T. (1953), Relative permeability calculations from pore size distribution data, *J. Pet. Technol.*, *5*(3), 71–78, doi:10.2118/225-G.

Celia, M. A., and J. M. Nordbotten (2009), Practical modeling approaches for geological storage of carbon dioxide, *Ground Water*, *47*(5), 627–638, doi:10.1111/j.1745-6584.2009.00590.x.

Chabora, E. R., and S. M. Benson (2009), Brine displacement and leakage detection using pressure measurements in aquifers overlying CO_2 storage reservoirs, *Energy Procedia*, *1*(1), 2405–2412, doi:10.1016/j.egypro.2009.01.313.

Chadwick, R. A., B. P. Marchant, and G. A. Williams (2014), CO_2 storage monitoring: Leakage detection and measurement in subsurface volumes from 3D seismic data at Sleipner, *Energy Procedia*, *63*, 4224–4239, doi:10.1016/j.egypro.2014.11.458.

Cihan, A., Q. Zhou, and J. T. Birkholzer (2011), Analytical solutions for pressure perturbation and fluid leakage through aquitards and wells in multilayered-aquifer systems, *Water Resour. Res.*, *47*, W10504, doi:10.1029/2011WR010721.

Hammond, G. E., P. C. Lichtner, and R. T. Mills (2014), Evaluating the performance of parallel subsurface simulators: An illustrative example with PFLOTRAN, *Water Resour. Res.*, *50*, 208–228, doi:10.1002/2012WR013483.

Hosseini, S. A. (2014), Time lapse compressibility monitoring for detection of CO_2 leakage in brine aquifers, *Energy Procedia*, *63*, 4459–4463, doi:10.1016/j.egypro.2014.11.481.

Hu, L., P. Bayer, P. Alt-Epping, A. Tatomir, M. Sauter, and R. Brauchler (2015), Time-lapse pressure tomography for characterizing CO_2 plume evolution in a deep saline aquifer, *Int. J. Greenhouse Gas Control*, *39*, 91–106, doi:10.1016/j.ijggc.2015.04.013.

Illman, W. A., J. Zhu, A. J. Craig, and D. Yin (2010), Comparison of aquifer characterization approaches through steady state groundwater model validation: A controlled laboratory sandbox study, *Water Resour. Res.*, *46*, W04502, doi:10.1029/2009WR007745.

Jung, Y., Q. Zhou, and J. T. Birkholzer (2013), Early detection of brine and CO_2 leakage through abandoned wells using pressure and surface-deformation monitoring data: Concept and demonstration, *Adv. Water Resour.*, *62*, 555–569, doi:10.1016/j.advwatres.2013.06.008.

Lee, S. J., B. J. McPherson, and F. G. Vasquez (2015), Leakage pathway estimation using iTOUGH2 in a multiphase flow system for geologic CO_2 storage, *Environ. Earth Sci.*, *74*(6), 5111–5128, doi:10.1007/s12665-015-4523-3.

Lemieux, J. (2011), Review: The potential impact of underground geological storage of carbon dioxide in deep saline aquifers on shallow groundwater resources. *Hydrogeol. J.*, *19*(4), 757–778, doi:10.1007/s10040-011-0715-4

Meckel, T. A., M. Zeidouni, S. D. Hovorka, and S. A. Hosseini (2013), Assessing sensitivity to well leakage from three years of continuous reservoir pressure monitoring during CO_2 injection at Cranfield, MS, USA, *Int. J. Greenhouse Gas Control*, *18*, 439–448, doi:10.1016/j.ijggc.2013.01.019.

Niemi, A., J. Bensabat, F. Fagerlund, M. Sauter, J. Ghergut, T. Licha, T. Fierz, G. Wiegand, M. Rasmusson, K. Rasmusson, et al. (2012), *Energy Procedia*, *23*, 504–511, doi:10.1016/j.egypro.2012.06.048.

Nogues, J. P., J. M. Nordbotten, and M. A. Celia (2011), Detecting leakage of brine or CO_2 through abandoned wells in a geological sequestration operation using pressure monitoring wells, *Energy Procedia*, *4*, 3620–3627, doi:10.1016/j.egypro.2011.02.292.

Nordbotten, J. M., M. A. Celia, and S. Bachu (2004), Analytical solutions for leakage rates through abandoned wells, *Water Resour. Res.*, *40*, W04204, doi:10.1029/2003WR002997.

Nordbotten, J. M., D. Kavetski, M. A. Celia, and S. Bachu (2008), Model for CO_2 leakage including multiple geological layers and multiple leaky wells, *Environ. Sci. Technol.*, *43*(3), 743–749, doi:10.1021/es801135v.

Park, Y. C., D. G. Huh, and C. H. Park (2012), A pressure-monitoring method to warn CO_2 leakage in geological storage sites, *Environ. Earth Sci.*, *67*(2), 425–433, doi:10.1007/s12665-012-1667-2

Sun, A. Y., and J.-P. Nicot (2012), Inversion of pressure anomaly data for detecting leakage at geologic carbon sequestration sites, *Adv. Water Resour.*, *44*, 20–29, doi:10.1016/j.advwatres.2012.04.006.

Sun, A. Y., J. Lu, and S. Hovorka (2015), A harmonic pulse testing method for leakage detection in deep subsurface storage formations, *Water Resour. Res.*, *51*, 4263–4281, doi:10.1002/2014WR016567.

Vasco, D. W., H. Keers, and K. Karasaki (2000), Estimation of reservoir properties using transient pressure data: An asymptotic approach, *Water Resour. Res.*, *36*(12), 3447–3465, doi:10.1029/2000WR900179.

Wang, Z., and M. J. Small (2014), A Bayesian approach to CO_2 leakage detection at saline sequestration sites using pressure measurements, *Int. J. Greenhouse Gas Control*, *30*, 188–196, doi:10.1016/j.ijggc.2014.09.011.

Wiese, B., J. Böhner, C. Enachescu, H. Würdemann, and G. Zimmermann (2010), Hydraulic characterisation of the Stuttgart formation at the pilot test site for CO_2 storage, Ketzin, Germany, *Int. J. Greenhouse Gas Control*, *4*, 960–971, doi:10.1016/j.ijggc.2010.06.013.

Yeh, T., and S. Liu (2000), Hydraulic tomography: Development of a new aquifer test method, *Water Resour. Res. 36*(8), 2095–2105, doi: 10.1029/2000WR900114.

Zhou, Q., J. T. Birkholzer, and C. F. Tsang (2009), A semi-analytical solution for large-scale injection-induced pressure perturbation and leakage in a laterally bounded aquifer–aquitard system, *Transp. Porous Media*, *78*(1), 127–148, doi:10.1007/s11242-008-9290-0.